

Nanoscale

Accepted Manuscript



This is an *Accepted Manuscript*, which has been through the Royal Society of Chemistry peer review process and has been accepted for publication.

Accepted Manuscripts are published online shortly after acceptance, before technical editing, formatting and proof reading. Using this free service, authors can make their results available to the community, in citable form, before we publish the edited article. We will replace this *Accepted Manuscript* with the edited and formatted *Advance Article* as soon as it is available.

You can find more information about *Accepted Manuscripts* in the [Information for Authors](#).

Please note that technical editing may introduce minor changes to the text and/or graphics, which may alter content. The journal's standard [Terms & Conditions](#) and the [Ethical guidelines](#) still apply. In no event shall the Royal Society of Chemistry be held responsible for any errors or omissions in this *Accepted Manuscript* or any consequences arising from the use of any information it contains.

**High-performance supercapacitor of vertically-oriented few-layer graphene with
high-density defects**

Jun Lei Qi, Xu Wang, Jing Huang Lin, Fu Zhang, Ji Cai Feng* and Wei-Dong Fei*

*State Key Laboratory of Advanced Welding and Joining, Harbin Institute of
Technology, Harbin 150001, China*

Nanoscale Accepted Manuscript

*Corresponding author: Tel. /fax: 86-451-86418146;

E-mail: fengjc@hit.edu.cn (J C Feng) and wdfei@hit.edu.cn(W-D Fei) ;

Abstract:

Pristine graphene with 3D structure is desired for use in graphene-based supercapacitors, yet the very poor wettability in water of such graphene has limited its practical application. Here we report a way to simultaneously realize 3D structure and good wettability in vertically-oriented few-layer graphene (VFG) grown by plasma-enhanced chemical vapor deposition. Based on scanning and transmission electron microscopic, Raman spectroscopic, contact angle (CA) and electrochemical analyses, a mechanism to explain the improved performance of VFG-based supercapacitors by defect-stimulated increases in wettability is proposed. The CA of our VFG samples notably reduces from 131° to 73° as the content of surface defects increases, which confirms that the wettability of VFG is markedly improved with an increased density of surface defects. Electrochemical results indicate that the VFG samples with a high density of defects exhibit high specific capacities of up to $704\mu\text{F}/\text{cm}^2$ and good cycling stability with about 91.2% capacitance retention after 3000 cycles. The excellent supercapacitor performance of the VFG samples with a high density of defects makes them attractive candidates as ultrathin high-performance supercapacitor electrodes.

1. Introduction

Electric double-layer capacitors (EDLC), also known as supercapacitors or ultracapacitors, are promising for energy storage because of advantages including high power capability, high cycle efficiency, long cycle life and being maintenance free.¹⁻⁵ Although tremendous progress has been made, the relatively low specific capacitance of EDLCs still limits their practical application. For example, carbon materials like activated carbon and carbon fibers with a high surface area, which have been widely used as electrode materials in EDLCs,^{6,7} possess EDLC capacitances of no more than $21\mu\text{F}/\text{cm}^2$, which is the intrinsic capacitance of pristine graphene.⁷⁻⁹ Recently, several studies^{3,7,10} have indicated that EDLC electrodes with 3D structure show markedly improved capacitance. The introduction of 3D structure could optimize ion diffusion, which minimizes charge recombination and storage channels as well as increasing specific surface area. Miller *et al.*¹ demonstrated that vertically-oriented few-layer graphene (VFG) electrodes grown by plasma-enhanced chemical vapor deposition (PECVD) on Ni substrates can greatly increase charge storage compared with that of designs that rely on basal plane surfaces. This finding is expected to direct the power management of future electronic devices, especially ultrathin ones because these VFG electrodes exhibit capacitance values as high as $50\text{-}70\mu\text{F}/\text{cm}^2$. Ajayan *et al.*³ reported that pristine graphene (1-2 layers) with an “in-plane” architecture where graphene was vertically-oriented to the current collectors possesses an EDLC capacitance of $80\mu\text{F}/\text{cm}^2$, whereas that of reduced multilayer graphene oxide (RMGO) with an “in-plane” architecture can reach up to $394\mu\text{F}/\text{cm}^2$. It is known that the electrical and mechanical properties of pristine graphene are far better than those of RMGO. However, the low capacitance obtained for pristine graphene (or VFG) of less than $100\mu\text{F}/\text{cm}^2$ does not reach its theoretical

maximum. Many researchers have reported that pristine graphene is very hydrophobic. VFG exhibits very poor wettability with water because of the hydrophobic nature of pristine graphene and its 3D structure.^{4, 8, 10-13} This poor wettability leads to low surface contact area between VFG and the electrolyte, which may impair the performance of VFG-based supercapacitors. Therefore, the incompatibility between 3D structure and wettability is a limitation of VFG-based supercapacitors.

Here we report a simple and effective way to simultaneously realize 3D structure and good wettability in VFG-based electrodes, overcoming the problems discussed above. The corresponding VFG-based supercapacitor exhibits ultra-high capacitance and cycle stability.

2. Experimental

VFG was synthesized *in-situ* on Pt substrates (200 nm-thick Pt film deposited on Si) by radio-frequency (RF) PECVD with a substrate temperature of 700°C in a mixture of CH₄, Ar and H₂ gases for 1h. The total gas pressure was fixed at 600Pa, and the RF power was 200W.

The morphology and structure of the obtained samples were characterized by scanning electron microscopy (SEM; JEOL JSM-6700F), transmission electron microscopy (TEM) and high-resolution TEM (HRTEM; JEOL TEM-2010 operated at 200kV), Raman spectroscopy (Renishaw-invia with an excitation wavelength of 532 nm) and X-ray photoelectron spectroscopy (XPS; ESCALAB 250Xi).

VFG-based supercapacitors were assembled in a two-electrode system with a layered structure and all the components were sandwiched between two pieces of plastic sheet.^{5, 14} Two pieces of 1 cm×1 cm VFG/Pt samples (The loading level of the VFG is about 0.001mg/cm²) were utilized as two porous electrodes which were isolated from electrical contact by a porous polypropylene film. The ultra-thin and organized arrays

of VFG/Pt work as a dual function layer where VFG nanosheets exposed to the electrolyte act as active electrodes and Pt substrates the current collectors.¹⁵ The separator (porous polypropylene film) and the electrodes were impregnated with 6 M KOH aqueous electrolyte solution, which allowed ionic transmission while preventing electronic current from discharging the cell.¹⁶ A platinum wire was clipped onto the end of each current collector.

Cyclic voltammetry (CV), galvanostatic charge/discharge (CD) and self-discharge testing were conducted in a three-electrode system containing an aqueous electrolyte solution of 6 M KOH within the potential window from -0.2 to 0.4 V vs. saturated calomel electrode. The obtained VFG/Pt samples were cut into 1 cm×1 cm and attached to the electrode holder acting as working electrode. 2 cm×1 cm platinum film was used as auxiliary electrode, and calomel electrode as reference electrode. These testing were operated by electrochemical workstation (CHI-760E). We carried out complex-plane electrochemical impedance spectrum (EIS) testing in the same three-electrode system by electrochemical workstation (PARSTAT 2273). EIS testing was performed at a DC bias of 0 V over a frequency range of 100 kHz to 100 mHz.

3. Results and discussion

Fig. 1 show SEM images of samples grown by PECVD with different gas flow rate ratios of CH₄/Ar/H₂ of 10/90/0, 10/87/3, 10/85/5, 10/82/8 and 10/80/10 sccm, respectively. The total gas flow rate was kept at 100 sccm, and the CH₄ gas flow rate was constant at 10 sccm. All of the samples contain uniform VFG that is vertically-oriented on the Pt substrate. The shape, size and density of the VFG grown using different gas atmospheres are almost the same. This suggests that a slight change of gas ratio of Ar:H₂ when other parameters are fixed will not trigger obvious morphology variation. This may be because the formation of C atoms in each process

reached an almost ‘saturated’ state¹⁷ because of the consistent, adequate supply of CH₄, so small fluctuations of Ar and H₂ did not have a large effect on the morphology of the VFG samples.

The side-view SEM, TEM and HRTEM images of the VFG samples deposited with a CH₄/Ar/H₂ ratio of 10/90/0 sccm (VFG@10/90/0) are presented in Fig. 2. Fig. 2a provides a good, visual perspective of the vertical growth of VFG on the substrate with densely exposed edge planes and random expansive open areas. The average size of VFG nanosheets is about 100 nm×100 nm. The thickness (height) of the VFG film is about 100 nm, as shown in Fig. 2a. The edge of VFG is sharp and transparent, which suggests these nanosheets are very thin (Fig. 2b). A selected area electron diffraction pattern (SAED) corresponding to the VFG is presented in the insert of Fig. 2b, which can be indexed to the (002), (100), (004) and (110) planes of polycrystalline graphite. This suggests that the as-grown VFG has graphite crystalline structure. In addition, the height of VFG nanosheets can be obtained from the cross-sectional view of VFG in TEM image (Fig. 2c) accurately. The complete VFG nanosheets were separated from substrate by mechanical exfoliation and the average net height of VFG nanosheets is estimated to be around 100 nm. The HRTEM image of a typical edge of VFG (Fig. 2d) reveals the graphite structure of the VFG with an interplanar spacing of 0.34 nm. The edge of the VFG is about 3-5 graphene layers thick.

Raman spectroscopic analysis of the samples was conducted to characterize the layer stacking and layer number of graphene.¹⁷⁻¹⁹ Raman spectra of the VFG grown with different gas flow rate ratios are illustrated in Fig. 3a. The Raman spectra of all of the samples contained three bands at 1350, 1585 and 2690 cm⁻¹ corresponding to the D, G and 2D bands, respectively. The G band represents the E_{2g} phonon at the center of the Brillouin zone, while the D and 2D bands are generated by double-resonant Raman

scattering.¹⁸ The intensity ratio of the 2D and G bands (I_{2D}/I_G) indicates the quality and layer number of graphene while the intensity ratio of the D to G bands (I_D/I_G) is related to the degree of disorder and defects in graphene.¹⁹

The Raman spectral analysis results are listed in Table 1. The I_{2D}/I_G ratio of the VFG@10/90/0 is about 0.7. This suggests that this VFG sample is few-layer graphene with an average thickness of between 3 and 10 atomic layers,^{19, 20} which corresponds well with the HRTEM results (Fig. 2d). This agreement confirms that the Raman spectrum gives us valid data for the thickness of the PECVD-grown VFG samples. Table 1 and Fig. 3b indicate that the I_{2D}/I_G ratios of all of the VFG samples are around 0.6-0.7, which suggests that the samples are all few-layer graphene of similar thickness. These values further demonstrate that the slight change of Ar and H₂ gas ratio during PECVD does not visibly change the morphology and thickness of the VFG. However, the I_D/I_G ratio of the PECVD-grown VFG samples varied from 1.4 to 2.0, which indicates that the degree of surface defects in the VFG samples is sensitive to slight changes of gas ratio. This sensitivity of surface defect formation to gas ratio may arise for the following reasons: on one hand, it is known that the growth of VFG by PECVD is through self-assembly, so the deposition of VFG involves the accumulation and incorporation of carbon radicals at the edges and sides of VFG.²¹ That is, the growth of VFG mainly depends on the content of carbon radicals in the reaction atmosphere. Thus, as light change of Ar and H₂ gas ratio would not trigger large morphology differences as long as sufficient C feedstock is provided. On the other hand, a high concentration of H radicals is unfavorable for carbon nanomaterial formation and growth, likely because sp² C is readily attacked by H radicals to form sp³ structures.^{22, 23} In our previous study,²⁴ as the Ar content of the reaction atmosphere increased, the degree of graphitization increased and the content of crystal

defects decreased in carbon nanomaterials. This is because the Ar ions can remove the amorphous carbon on the surfaces of carbon nanomaterials during PECVD. Therefore, the content of crystal defects increases in the PECVD-grown VFG as H₂ content increases and Ar content decreases in a CH₄/Ar/H₂ atmosphere.

XPS was performed to further analyze the chemical composition and valence states of the VFG samples. The XPS spectrums of all samples mainly consist of a strong C 1s peak at 284 eV and a relatively weak O 1s peak at 533 eV,^{18, 25-27} as shown in Fig. 4. The atomic concentration for C and O in all samples is estimated to be 98% and 2% respectively, indicating that few oxygen-doped defects or oxygen functional groups exist in VFG samples. This slight contamination is mainly attributed to C-O and C=O formed by physical or chemical adsorption at the surface of VFG nanosheets when exposed to ambient conditions.²⁸ This result suggests that the existence of small amounts of oxygen-doped defects or oxygen functional groups has little (approximately the same) effect on the degree of defects in VFG.

To further investigate the state of the surface defects in VFG, the HRTEM images and C1s XPS spectra for VFG samples (VFG@10/90/0 and VFG@10/80/10) are presented in Fig. 5. It is clear to see that the edges of both VFG samples are integral and very smooth with orderly arrangement of atoms when comparing the HRTEM results of VFG@10/90/0 and VFG@10/80/10 in Fig. 5a and 5d. It suggests that the edges of both VFG samples are almost the same with slight defects. However, the sheet-plane of both VFG samples is quite different, as shown in Fig 5b and 5e. It can be found that the crystal structure of the sheet-plane in VFG@10/90/0 is more ordered than that in VFG@10/80/10, indicating a relatively low degree of surface defects in VFG@10/90/0. These results also reveal that the increased defects are located on the sp² plane of VFG nanosheets.

High-resolution C 1s XPS spectrum of VFG@10/90/0 and VFG@10/80/10 are presented in Fig. 5c and 5f. The VFG signal shows the main C sp² peaks with an obvious shoulder on the high binding energy side. Only ~2 atm.% oxygen was estimated to be present on the basis of the XPS analysis (Fig. 4), which indicates that the C-O peak should not be the origin of this peak shoulder.¹⁸ The asymmetric C 1s peak can be decomposed into a main peak at 284.6 eV (C sp²) originating from the sp²-hybridized carbon bonding of graphene and a weak peak at 285.4 eV (C sp³) which is attributed to the sp³-hybridized carbon bonding or structural defects of graphene.^{18, 25, 26} Moreover, the atomic ratio of C sp² and C sp³ is related to the degree of graphitization or defect of graphene.^{25, 27} The atomic ratio of C sp² and C sp³ is obtained by taking the ratio of the C 1s peak areas in XPS spectra. As shown in Fig. 5c and 5f, the peak area ratio of C sp²/C sp³ in VFG@10/90/0 (~18.94) is much higher than that in VFG@10/80/10 (~6.75). This result suggests that the VFG@10/90/0 have a lower density of defects and a higher degree of graphitization than VFG@10/80/10, which corresponds well with the HRTEM and Raman results.

We next characterized the wettability of the PECVD-grown VFG towards water. The static contact angles of water droplets on the VFG samples were measured by standing a droplet of deionized water (2μL) on the sample surface. As shown in Table 1, the contact angles of VFG@10/90/0, 10/87/3, 10/85/5, 10/82/8 and 10/80/10 were 131°, 112°, 98°, 85° and 73°, respectively. It is noteworthy that the effect of surface roughness in conjunction with the surface chemistry of the VFG gives a highly hydrophobic surface.^{18, 29} High-quality graphene-coated metal substrates always show contact angles of 80-90°,²² so the VFG-deposited Pt substrate in our experiment with a CH₄/Ar/H₂ gas flow rate ratio of 10/90/0 sccm exhibits even worse wettability than defect-free graphene-coated Pt. It has been suggested that the interaction between 3D

structural morphology and the hydrophobic nature of graphene might decrease the wettability of the substrate surface.²⁹ The poor wettability of VFG samples with a low density of defects might limit the advantage of 3D structure in the formation of EDLCs. However, the contact angles of water droplets on the VFG samples decrease as the content of surface defects increases (Table 1). This suggests that a correlation exists between the degree of surface defects and wettability of VFG. The surface energy of graphene is increased as more defects are present.^{13, 30} Hydrophilicity is achieved when the attraction between a polarized lattice and water molecules is stronger than the interaction between water molecules.^{13,18} The contact angles of water droplets on VFG are correlated with the degree of defects; the wettability improves as the degree of defects increases. In other words, the content of surface defects can be modified to control the wettability of graphene.

The PECVD-grown VFG samples were examined as electrode materials by standard cyclic voltammetry (CV) and galvanostatic charge/discharge testing. The specific capacitance of each VFG electrode (C_{VFG}) was calculated; the results are shown in Table 1 and Fig. S1. C_{VFG} at a scan rate of 2mV/s are 263, 333, 393, 536 and 704 $\mu\text{F}/\text{cm}^2$ for the VFG@10/90/0, 10/87/3, 10/85/5, 10/82/8 and 10/80/10, respectively. C_{VFG} increases as the degree of defects in VFG increases and the contact angles of water droplets on VFG decrease (Table 1). These results suggest that C_{VFG} strongly depends on the degree of defects and wettability of the VFG sample.

Fig. 6a depicts CV curves of the VFG@10/80/10 measured at scan rates of 2, 5, 10, 20 and 50 mV/s. The CV curve area gradually enlarged as the scan rate increased, and maintained its quasi-rectangular shape even at a scan rate of 50 mV/s, consistent with EDLC behavior.⁸ At a scan rate of 2mV/s, this VFG sample with a high density of defects demonstrated an ultra-high specific capacitance of 704 $\mu\text{F}/\text{cm}^2$. Because the

VFG had a height of around 100nm, the highest specific capacitance of the VFG-based supercapacitor was calculated to be 70 F/cm^3 , which is high performance in current works.^{1, 3, 7, 38} The electrochemical cycling stability of the VFG@10/80/10 was examined by charge-discharge cycling at a current density of 0.1 mA/cm^2 , as shown in Fig. 6b. C_{VFG} exhibited good stability, retaining about 91.2% of the original capacitance after 3000 cycles. In addition, the cycling stability of VFG@10/90/0, 10/87/3, 10/85/5 and 10/82/8 is excellent as well with capacitance retention all above 90% after 3000 cycles, as shown in Fig. S2. This stability demonstrates that the VFG with a high density of defects could be a promising candidate for ultrathin high-performance supercapacitor electrodes.

In order to understand the dielectric and transport properties of the VFG electrodes, electrochemical impedance spectrum (EIS) was carried out in three-electrode symmetrical system. Fig. 7a shows the Nyquist plots for all samples obtained in 6 M KOH at a DC bias of 0 V over a frequency ranges of 100 kHz to 100 mHz. It is clear to see that the shape and variation tendency of all curves are approximately the same. The near-vertical curves indicate a good double-layer capacitor behavior.^{31, 32} It is the representative of the ion diffusion in the electrode structure. The more vertical the curve, the more closely the supercapacitor behaves as an ideal capacitor.^{8, 33} More details of the curves can be observed in the insert of Fig. 7a. The semicircle at the high frequency is nearly invisible, suggesting a significantly small interfacial charge-transfer resistance (R_{ct}) in active materials (VFG). The 45° sloped portion of the Nyquist plots at the end of low-frequency region indicates a porous electrode behavior.¹ It is mainly associated with the non-stacked 3D-structured VFG nanosheets and defects at the surface of nanosheets which can facilitate efficient access for ion diffusion. The slight difference of each curve in this region is due to the correlation

between the degree of defects and wettability. Increased exterior defects can provide favorable wettability for VFG, which leads to excellent electrical conductivity inside electrodes.

Fig. 7b shows the Nyquist plots for Pt substrate and VFG@10/80/10 at the same parameters. Compared with VFG@10/80/10 on Pt substrate, the Pt substrate exhibits a near-vertical curve in both low-frequency region and high-frequency region (Black curve in Fig. 7b). The equivalent series resistance (ESR) of Pt substrate and VFG@10/80/10 is around 1.30 Ω and 1.45 Ω , respectively, which are calculated from the intersecting point with the x-axis in the range of high frequency,³⁴ including the electrolyte resistance, the intrinsic resistance of the active electrode material, and the contact resistance at the interface of the active material and the current collector.^{35,36} From the different ESR between two samples, the intrinsic resistance and contact resistance of VFG can be estimated to be 150 m Ω , indicating that the VFG has good ion response at high-frequency ranges. The low resistance (150 m Ω) suggests that the contact resistance between VFG and Pt substrate in the VFG/Pt prepared by *In-situ* growth is relatively low. Moreover, the ESR of all VFG samples remain the same (around 1.45 Ω) as shown in the inset of Fig. 7a, suggesting that the enhancement of supercapacitor performance is mainly attributed to the effect of intrinsic defects of VFG which facilitates the efficient access of ion diffusion in VFG-aqueous electrolyte system.

The above results reveal that a correlation exists between the degree of defects, wettability and supercapacitor properties of VFG. Fig. 8 shows the contact angles and specific capacitance of VFG with different I_D/I_G ratios. Both C_{VFG} and contact angle strongly depend on the I_D/I_G ratio. As the I_D/I_G ratio increases, the contact angle decreases, and C_{VFG} increases. This indicates that surface defects play an important

role in improving the performance of VFG-based supercapacitors. Furthermore, it is well known that the performance of carbon-based supercapacitor can be enhanced by improving their wettability. Therefore, we believe that the high performance of our VFG-based supercapacitors is achieved by the defects improving wettability.

To reveal the enhancement mechanism of the performance of our VFG-based supercapacitors by defect-stimulated wettability increase, we schematically elucidated the correlation between the degree of defects, wettability and supercapacitor performance of the VFG samples, as shown in Fig. 9. Fig. 9a illustrates the VFG sample with a low density of defects (high-quality graphene) oriented vertically on a Pt substrate. It is evident that the non-stacking 3D-structured VFG nanosheets are used to optimize ion diffusion and storage channels as well as increasing the effective surface area that is electrochemically accessible.⁸ However, this VFG sample with a low density of defects is poorly wetted by aqueous electrolyte, hindering the formation of electric double-layer capacitance, which unexpectedly limits the advantage of 3D structure for supercapacitor applications. For this reason, improvement of the wettability between electrode and electrolyte is important for VFG-based supercapacitors. As shown in Fig. 9b, the VFG with a high density of defects is easily wetted with electrolyte because of its relatively high surface energy. The favorable wettability between this VFG sample and electrolyte increases the effective surface area with 3D morphology, which results in high capacitance during electrochemical testing.

In-situ growth studies have suggested that graphene formed earlier that is located in the interior of the sample lacks defects.^{17, 37} In contrast, the outer graphene surface has a relatively low proportion of graphitization with a large content of inter-crystalline defects, perhaps because of the strong ion bombardment during the process. Unlike

the attached defects and damaged structure of chemically converted graphene,^{4,31} these intrinsic surface defects can introduce plentiful charge carriers into the 2D network of VFG, which might underpin the excellent electrical conductivity of graphene.¹⁸ It is known that the surface defects of VFG could not substantially enhance C_{VFG} . Thus, the marked enhancement of C_{VFG} can be attributed to the defect-stimulated increase in the wettability of VFG. In addition, the negligible contact resistance between VFG and the Pt substrate and the excellent conductivity of the Pt electrode might also be responsible for the ultra-high specific capacitance of the VFG electrode with a high defect content.

Based on the above results and discussion, we believe that a defect-stimulated increase in wettability is a simple and effective way to produce high-performance graphene-based supercapacitor electrode materials. In our case, the ultra-high performance of the VFG-based supercapacitor is attributed to the following reasons: (1) the morphology of the non-stacked 3D-structured VFG nanosheets optimizes ion diffusion and storage channels as well as increasing the effective surface area. (2) The favorable wettability of VFG with a high density of defects increases the effective surface area of the 3D-structured morphology by increasing electrode-electrolyte interaction. (3) The high-quality interior and defect-rich exterior of the VFG lead to excellent electrical conductivity. (4) The use of Pt as a substrate material increases electrical conductivity.

4. Conclusions

We found the defect-stimulated increases in wettability allowed simultaneous realization of 3D structure and good wettability in VFG-based supercapacitor electrodes. A correlation between the degree of defects, wettability and supercapacitor properties of VFG was demonstrated. Our results confirm that defects in VFG

increase its wettability, inducing high capacitance of up to $704\mu\text{F}/\text{cm}^2$. VFG with a high density of defects shows promise for use as an ultrathin high-performance supercapacitor electrode.

Acknowledgement

The support from the National Natural Science Foundation of China (Grant Nos 51105108), and the Fundamental Research Funds for the Central Universities (Grant No. HIT. NSRIF. 2010113), China, is highly appreciated.

References

1. J. R. Miller, R. A. Outlaw and B. C. Holloway, *Science*, 2010, 329, 1637.
2. H. X. Ji, X. Zhao, Z. H. Qiao, J. Jung, Y. W. Zhu, Y. L. Lu, L. L. Zhang, A. H. MacDonald and R. S. Ruoff, *Nature communications*, 2014, 5, 3317.
3. J. J. Yoo, K. Balakrishnan, J. S. Huang, V. Meunier, B. G. Sumpter, A. Srivastava, M. Conway, A. L. M. Reddy, J. Yu, R. Vajtai and P. M. Ajayan, *Nano Lett.*, 2011, 11, 1423.
4. K. Zhang, L. Mao, L. L. Zhang, H. S. O. Chan, X. S. Zhao and J. S. Wu, *J. Mater. Chem.*, 2011, 21, 7302.
5. Z. Bo, W. G. Zhu, W. Ma, Z. H. Wen, X. R. Shuai, J. H. Chen, J. H. Yan, Z. H. Wang, K. F. Cen and X. L. Feng, *Adv. Mater.*, 2013, 25, 5799.
6. L. Zhao, L. Z. Fan, M. Q. Zhou, H. Guan, S. Qiao, M. Antonietti and M. M. Titirici, *Adv. Mater.*, 2010, 22, 5202.
7. Z. Bo, Z. H. Wen, H. Kim, G. H. Lu, K. Yu and J. H. Chen, *Carbon*, 2012, 50, 4379.
8. C. G. Liu, Z. N. Yu, D. Neff, A. Zhamu and B. Z. Jang, *Nano Lett.*, 2010, 10, 4863.
9. J. L. Xia, F. Chen, J. H. Li and N. J. Tao, *Nat. Nanotechnol.*, 2009, 4, 505.
10. Z. H. Wen, X. C. Wang, S. Mao, Z. Bo, H. Kim, S. M. Cui, G. H. Lu, X. L. Feng and J. H. Chen, *Adv. Mater.*, 2012, 24, 5610.
11. D. S. Yu, T. Kuila, N. H. Kim, P. Khanra and J. H. Lee, *Carbon*, 2013, 54, 310.
12. B. P. Jia and L. D. Zou, *J. Phys. Chem. Lett.*, 2012, 548, 23.
13. Y. J. Shin, Y. Y. Wang, H. Huang, G. Kalon, A. T. S. Wee, Z. X. Shen, C. S. Bhatia and H. Yang, *Langmuir*, 2010, 26, 3798.
14. Y. W. Zhu, S. Murali, M. D. Stoller, K. J. Ganesh, W. W. Cai, P. J. Ferreira, A. Pirkle, R. M. Wallace, K. A. Cychosz, M. Thommes, D. Su, E. A. Stach and R. S.

- Ruoff, *Science*, 2011, 332, 1537.
15. H. Y. Jung, M. B. Karimi, M. G. Hahm, P. M. Ajayan and Y. J. Jung, *Sci. Rep.*, 2012, 2, 773.
 16. M. D. Stoller, S. J. Park, Y. W. Zhu, J. H. An and R. S. Ruoff, *Nano Lett.*, 2008, 8, 3498.
 17. Z. Bo, Y. Yang, J. H. Chen, K. H. Yu, J. H. Yan and K. F. Cen, *Nanoscale*, 2013, 5, 5180.
 18. C. Y. Yang, H. Bi, D. Y. Wan, F. Q. Huang, X. M. Xie and M. H. Jiang, *J. Mater. Chem.*, 2013, A1, 770.
 19. A. C. Ferrari, J. C. Meyer, V. Scardaci, C. Casiraghi, M. Lazzeri, F. Mauri, S. Piscanec, D. Jiang, K. S. Novoselov, S. Roth and A. K. Geim, *Phys. Rev. Lett.*, 2006, 97, 187401.
 20. C. Casiraghi, S. Pisana, K. S. Novoselov, A. K. Geim and A. C. Ferrari, *Appl. Phys. Lett.*, 2007, 91, 23310891.
 21. I. B. Denysenko, S. Xu, J. D. Long, P. P. Rutkevych, N. A. Azarenkov and K. Ostrikov, *J. Appl. Phys.*, 2004, 95, 2713.
 22. A. Okita, Y. Suda, A. Oda, J. Nakamura, A. Ozeki, K. Bhattacharyya, H. Sugawara and Y. Sakai, *Carbon*, 2007, 45, 1518.
 23. G. Y. Zhang, D. Mann, L. Zhang, A. Javey, Y. M. Li, E. Yenilmez, Q. Wang, J. P. McVittie, Y. Nishi, J. Gibbons and H. J. Dai, *PNAS*, 2005, 102, 16141.
 24. J. L. Qi, X. Wang, H. W. Tian, Y. S. Peng, C. Liu and W. T. Zheng, *Journal of Alloys and Compounds*, 2009, 486, 265.
 25. R. A. Quinlan, M. Z. Cai, R. A. Outlaw, S. M. Butler, J. R. Miller and A. N. Mansour, *Carbon*, 2013, 64, 92
 26. C. M. Zhao, X. Wang, S. M. Wang, Y. Y. Wang, Y. X. Zhao and W. T. Zheng, *Int.*

- J. Hydrogen Energy*, 2012, 37, 11846.
27. S. M. Wang, Y. H. Pei, H. Wang, Q. N. Meng, H. W. Tian, X. L. Zheng, W. T. Zheng and Y. C. Liu, *J. Phys. D: Appl. Phys.*, 2010, 43, 455402.
28. L. L. Jiang, T. Z. Yang, F. Liu, J. Dong, Z. H. Yao, C. M. Shen, S. Z. Deng, N. S. Xu, Y. Q. Liu and H. J. Gao, *Adv. Mater.*, 2013, 25, 250.
29. S. B. Tian, L. Li, W. N. Sun, X. X. Xia, D. Han, J. J. Li and C. Z. Gu, *Sci. Rep.*, 2012, 2, 511.
30. J. Rafiee, X. Mi, H. Gullapalli, A. V. Thomas, F. Yavari, Y. F. Shi, P. M. Ajayan and N. A. Koratkar, *Nat. Mater.*, 2012, 11, 217.
31. L. L. Zhang, X. Zhao, M. D. Stoller, Y. W. Zhu, H. X. Ji, S. Murali, Y. P. Wu, S. Perales, B. Clevenger and R. S. Ruoff, *Nano Lett.*, 2012, 12, 1806.
32. Y. Y. Li, Z. S. Li and P. K. Shen, *Adv. Mater.*, 2013, 25, 2474.
33. Y. Wang, Z. Q. Shi, Y. Huang, Y. F. Ma, C. Y. Wang, M. M. Chen and Y. S. Chen, *J. Phys. Chem.*, 2009, 113, 13103.
34. C. M. Zhao, W. T. Zheng, X. Wang, H. B. zhang. X. Q. Cui and H. X. Wang, *Sci. Rep.*, 2013, 3, 2986
35. D. C. Zhang, X. Zhang, Y. Chen, P. Yu, C. H. Wang and Y. W. Ma, *J. Power Sources*, 2011, 196, 5990.
36. X. Li, J. P. Rong and B. Q. Wei, *ACS Nano*, 2010, 4, 6039.
37. T. Mori, M. Hiramatsu, K. Yamakawa, K. Takeda and M. Hori, *Diamond & Related Materials*, 2008, 17, 1513.
38. M. G. Hahm, R. A. M. Reddy, D. P. Cole, M. Rivera, J. A. Vento, J. Nam, H. Y. Jung, Y. L. Kim, N. T. Narayanan, D. P. Hashim, C. Galande, Y. J. Jung, M. Bundy, S. Karna, P. M. Ajayan and R. Vajtai, *Nano Lett.*, 2012, 12, 5616.

Table captions:

Table 1 The I_D/I_G ratio, I_{2D}/I_G ratio, Contact angle and C_{VFG} @ 2mV/s of the VFG at different gas flow rate ratios of CH₄/Ar/H₂.

	CH ₄ /Ar/H ₂ (sccm)				
	10/90/0	10/87/3	10/85/5	10/82/8	10/80/10
I_D/I_G ratio	1.46	1.58	1.68	1.85	2.05
I_{2D}/I_G ratio	0.70	0.68	0.66	0.64	0.63
Contact angle (°)	131	112	98	85	73
C_{VFG} @ 2mV/s ($\mu\text{F}/\text{cm}^2$)	263	333	393	536	703

Figure captions:

Figure 1 SEM images of VFG at the gas rate ratio ($\text{CH}_4/\text{Ar}/\text{H}_2$) of (a) 10/90/0, (b) 10/87/3, (c) 10/85/5, (d) 10/82/8 and (e) 10/80/10, respectively.

Figure 2 (a) side-view SEM, (b) TEM and corresponding SAED, (c) cross-sectional view TEM and (d) HRTEM image for VFG@10/90/0.

Figure 3 (a) Raman spectra, (b) I_D/I_G and I_{2D}/I_G ratio of the VFG@10/90/0, 10/87/3, 10/85/5, 10/82/8 and 10/80/10, respectively.

Figure 4 XPS spectrums for VFG at different $\text{CH}_4/\text{Ar}/\text{H}_2$ ratio.

Figure 5 HRTEM images and C 1s XPS spectrums of (a, b, c)VFG@10/90/0 and (d, e, f)VFG@10/80/10.

Figure 6 (a) the CV curves of the VFG @10/80/10 at the scanning rates of 2, 5, 10, 20 and 50 mV/s, (b) Cyclic stability obtained by performing charge-discharge of the VFG supercapacitor at $0.1\text{mA}/\text{cm}^2$ over 3000 cycles. It is apparent that the materials retain good stability over large number of charging-discharging cycles, in which the inset is the galvanostatic charge-discharge curve of the VFG supercapacitor.

Figure 7 (a) Nyquist plots for VFG deposited with different $\text{CH}_4/\text{Ar}/\text{H}_2$ ratios. Inset: magnified portion of the Nyquist plots near the origin. (b) Nyquist plots for Pt substrate and VFG@10/80/10.

Figure 8 the contact angles and specific capacitance of VFG with different I_D/I_G ratios

Figure 9 Schematic illustration of wettability of VFG with (a) low density defects and (b) high density defects. Inset photographs exhibit the water droplets on the substrate.

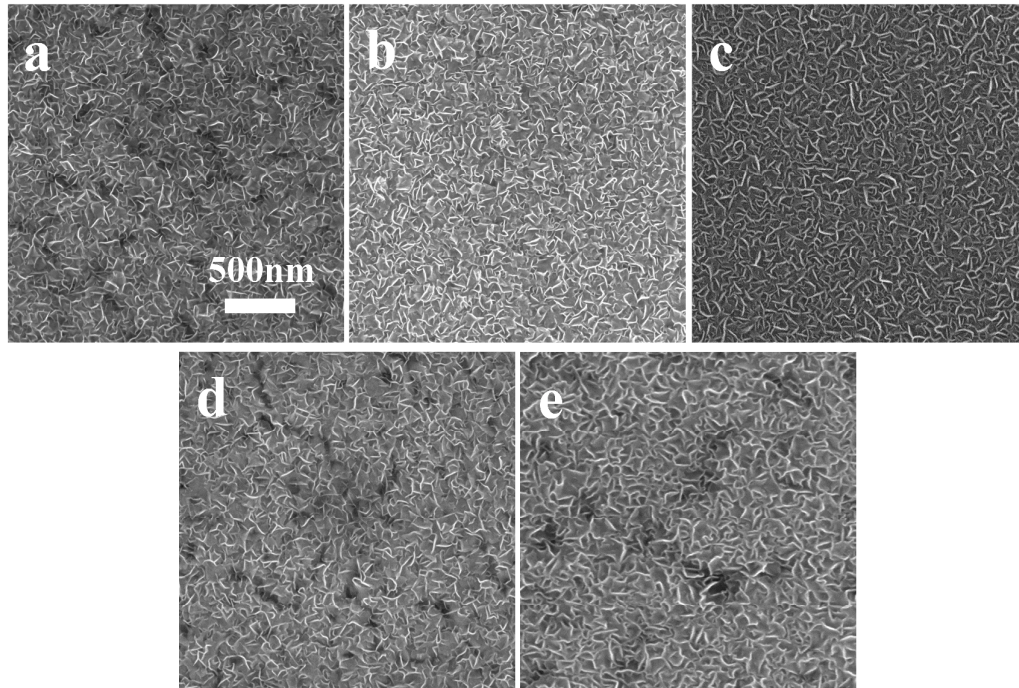


Fig. 1

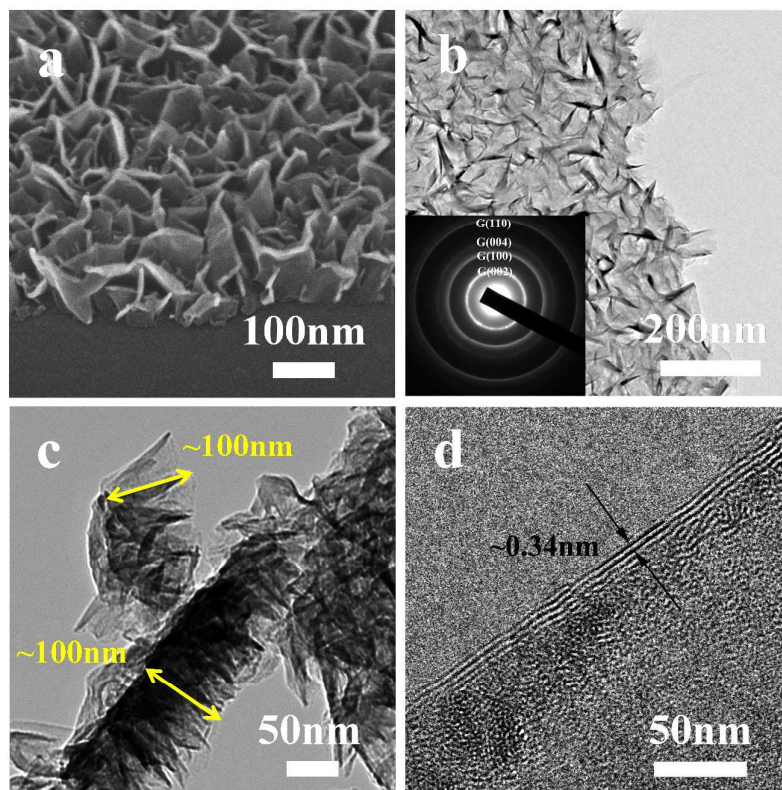


Fig. 2

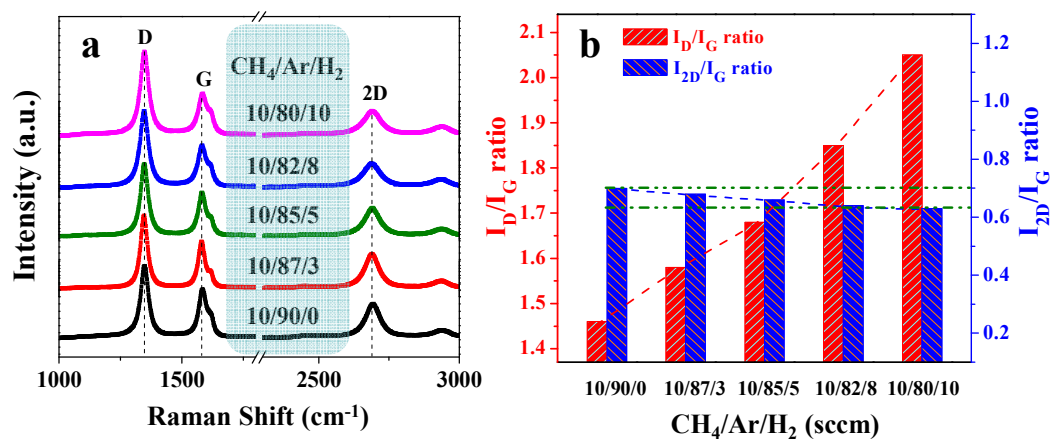


Fig. 3

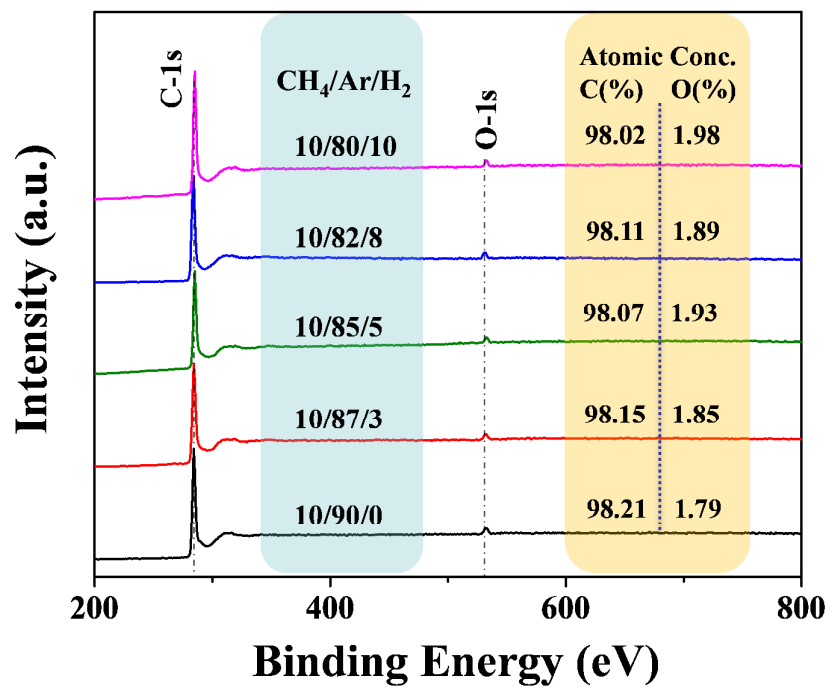


Fig. 4

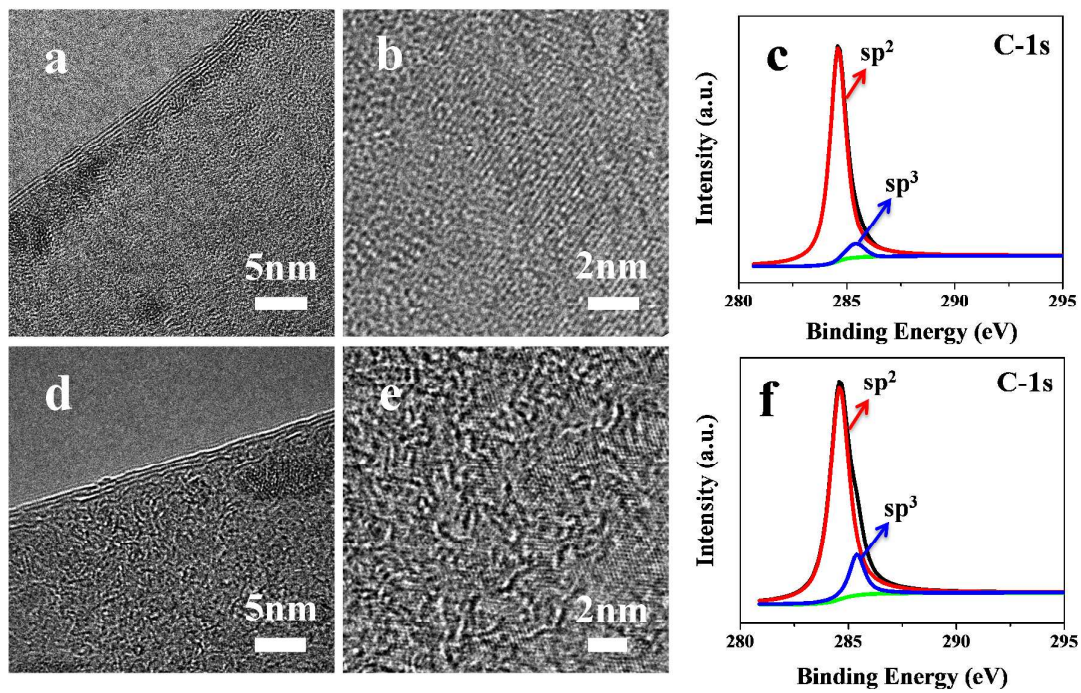


Fig. 5

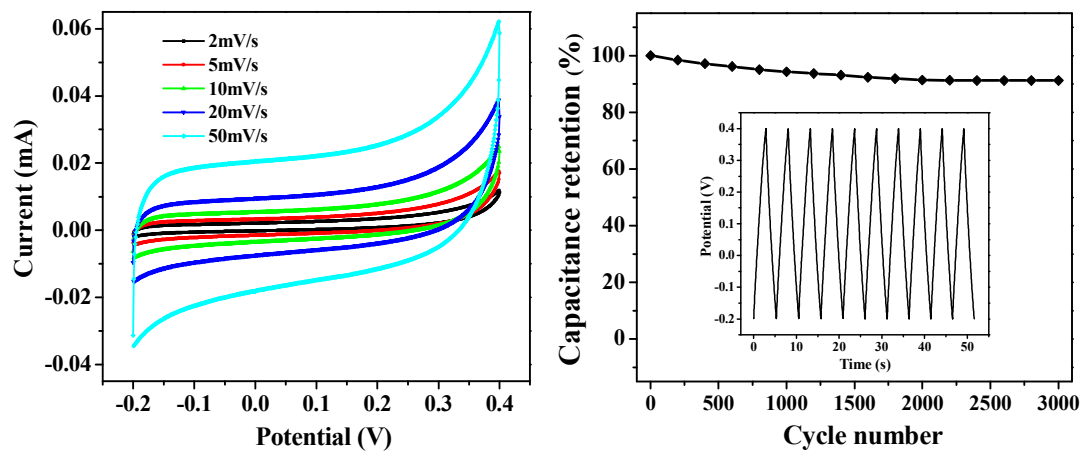


Fig. 6

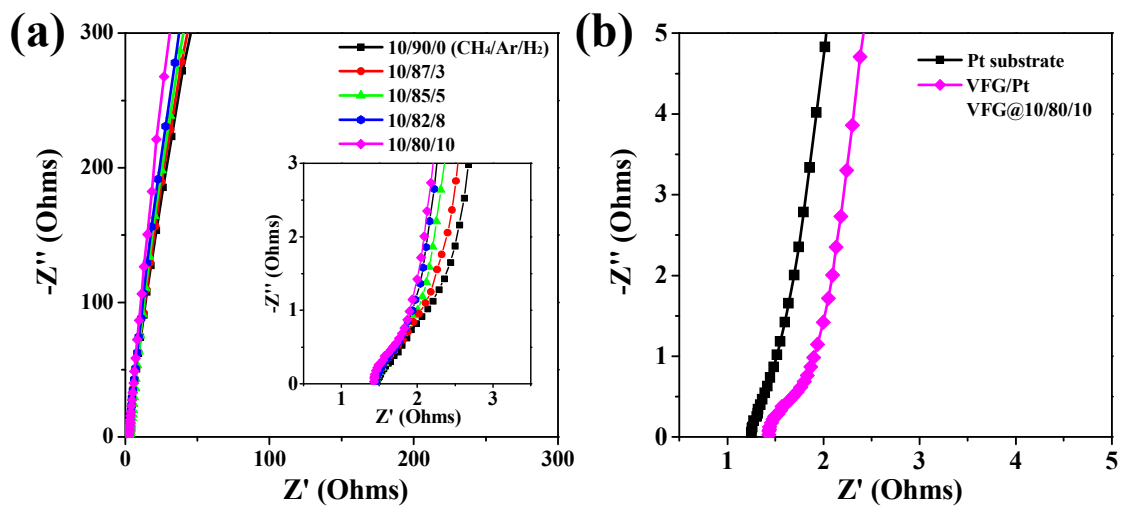


Fig. 7

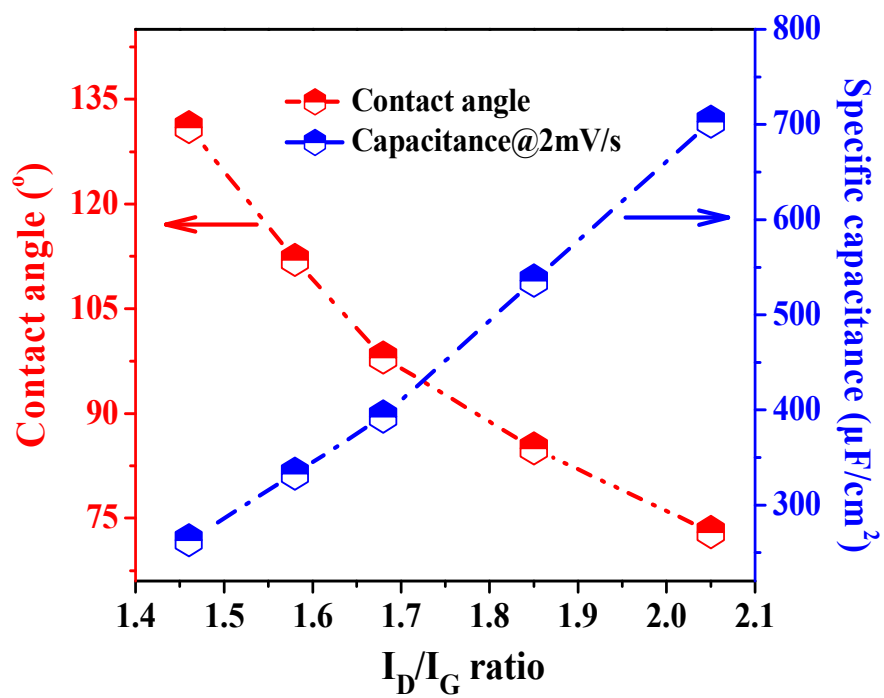


Fig. 8

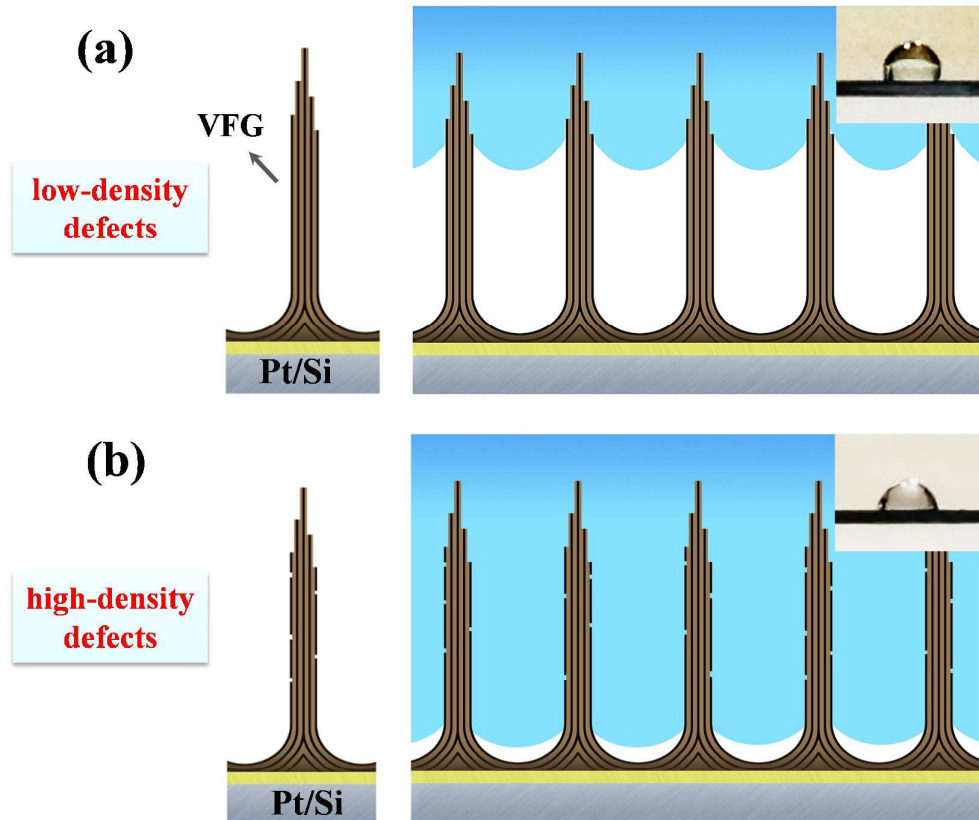


Fig. 9